Molecular Dynamics Simulations of Copper Binding to N-terminus Mutants of Amyloid-β

Oliver D. Kennedy-Britten, Nadiyah Al-Shammari, and James A. Platts*

School of Chemistry, Cardiff University, Park Place, Cardiff CF10 3AT, UK.

* Author for correspondence:

Email: platts@cardiff.ac.uk Phone: +44-2920-874950

Abstract

We report results of molecular dynamic (MD) simulations on N-terminus mutants of the copper-bound, amyloid-β (Aβ) peptide. Eight structures of Aβ were modelled, including seven mutant peptides in addition to the unaltered wild-type (WT). Trajectories analysed for each individual system were all approximately 1.4 μs in length, yielding a total of over 11 μs in total. The impact of these mutations are marked and varied compared to the wild-type peptide, including effects on secondary structure, stability and conformational changes. Each system showed differing levels of stability with some showing consistent, compact conformations whereas others displayed more flexible structures. Contrasts between comparable mutations at similar sites, such as A2T/A2V and D7H/D7N, show the location as well as the type of mutation have effects on protein structure observed in Ramachandran plots. We also report notable changes in peptide structure at residues remote to the site of substitution showing these mutations influence the entirety of Aβ**.** Salt-bridge profiles show this most clearly: addition or removal of charged residues affecting all salt-bridge interactions present in WT, even those remote from the site of mutation. Effects on secondary structure differ between mutations, most notably a change in incidence of β-strand, which has been linked to enhanced aggregational properties for the peptide. GFN2-xTB semi-empirical calculations show clear differences in binding energies of the copper-centre for each system.

Introduction

Alzheimer's disease (AD) is a progressive neurodegenerative disease accounting for two-thirds of all dementia diagnoses[1,2]. Projections estimate the total number of people afflicted with this condition globally will be approximately 42 million in 2020[3] causing great strain on patients, families and the healthcare system. Characteristic neurofibrillary tangles and plaques comprised of insoluble amyloid-β (Aβ) are key to AD diagnosis[4,5], along with increased levels of transition metals[6,7]. These deposits are a hallmark of AD pathology, in addition to levels of soluble Aβ oligomeric precursor species which have been associated with neurotoxicity[8,9].

Cases of dementia are commonly inferred to be a standard occurrence as part of the ageing process. Yet symptoms and diagnosis have also been observed in younger individuals (< 65 years old[10]) due to genetic alterations in the amino acid sequence of Aβ[11]. These instances of AD are referred to as early-onset familial Alzheimer's disease (EOFAD), and account for 5% of AD diagnoses[12]. We focused on 7 known mutations within the N-terminus of Aβ[13,14] (Figure 1). Some mutants cause an increase in production of the peptide from its precursor protein[15] (APP) such as E11K[16]. Increased pathogenicity has also been observed in A2V[17] and K16N[18] carriers via recessive and dominant-heterozygous genotypes respectively. Conversely, protective variants show an overall decrease in amyloidogenesis, such as in the case of A2T[19]. Unmutated, wild-type Aβ is hereby referred to as WT.

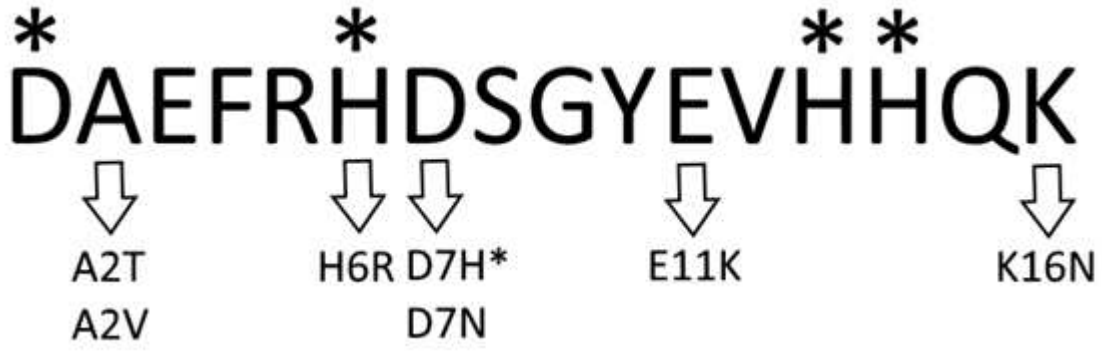

Figure 1 Amino acid sequence for N-terminal of WT, highlighting 7 known mutations; residues associated with coordination of Cu(II) are highlighted with an asterisk.

Naturally occurring ions such as Zn(II), Fe(II) and Cu(II) have a proclivity to bind to a range of

biological ligands, granting them high affinity for Aβ[20], particularly through nucleophilic residues such as His (at positions 6, 13 and 14) and Asp (position 1)[21]. Cu(II) binds to Aβ via a distorted square-planar complex at the N-terminal 1-16 residues of Aβ[22]. Coordination of copper can lead to generation of reactive oxidative species (ROS) which in turn encourage formation of intermolecular crosslinks between metallo-proteins[23,24]. These metal-peptide complexes, accompanied by a disruption in production and clearance of Aβ[25,26], lead to enhanced aggregation and subsequent formation of cerebral neurotoxic species[27,28]. Certain mutations can provide alternative modes of bonding to metals such as copper or zinc; replacement of metal-binding histidine in H6R[29], or the addition of another histidine in the D7H variant[30] are particularly notable in this context. These mutants, as well as D7N[31] substitution, are found to affect secondary structure and rates of formation of neurotoxic structures of Aβ[32].

An increase in β-character in the secondary structure of the Aβ peptide has been linked with an enhanced proclivity for aggregation[33]. Molecular dynamics (MD) seems a suitable choice for investigating the interactions and structures of this protein when bound with Cu(II), which has additionally been linked with increased formation of oligomeric and fibrous Aβ. Cu(II), as mentioned previously, binds within the first 16 residues of Aβ so this N-terminus can be used as a model for the full-length peptide. Similar computational studies have shown N-termini of Aβ peptides to be effective models to make inferences on interactions and structures of full-length Aβ[34,35].

In order to study effects of these mutants when coordinated to Cu(II), and to compare to the unaltered WT, we report the results of molecular dynamics simulations on Cu(II)-bound, truncated mutant and WT peptides noted in Figure 1. This allows us to draw comparisons on secondary structure and stability. From this, we can sample conformations and energies of each mutant system, and in doing so make inferences on aggregation behaviour compared against literature.

Computational Methods

Aβ1–16 was constructed in an extended conformation in MOE[36], with appropriate protonation states for physiological pH. Cu was coordinated to the peptides as shown in

Figure 2 via Asp1, His6, and His13, *i.e.* component I[37]. His14 could have been used in place of His13 but we made the decision to choose one of these residues for consistency across all simulations. The exception to this was H6R, which was bound via Asp1, His13 and His14[38] in the absence of His6. All constructed peptides were subjected to brief LowMode[39] conformational search to obtain starting structures. MD simulations were performed using the AMBER16[40] package. The AMBER ff14SB[41] forcefield parameter set was used to model all standard amino acid residues, while parameters for the metal and bound residues were obtained using the MCPB.py program[42]. Here, parameters are obtained from B3LYP/6-31G(d), and RESP charges for the metal-coordinating regions were obtained at the same level of theory using Gaussian09[43]. Semi-empirical calculations used the GFN2-XTB method[44] within Grimme's xtb package[45].

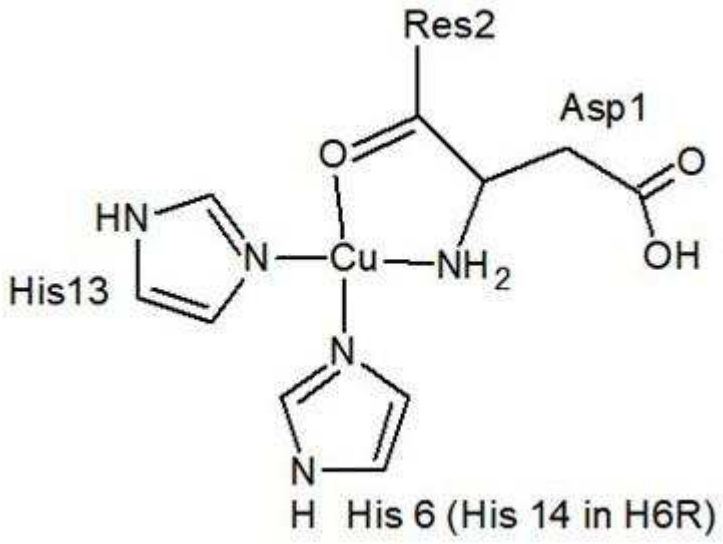

Figure 2 Coordination mode of Cu(II) to Aβ modelled across all simulations

The geometry of each system was optimised using 1000 steps of steepest descent and 1000 steps of conjugate gradient methods. MD simulations were carried out in the NVT ensemble, using a Langevin thermostat to control the temperature at 310 K. Three separate 500 ns MD simulations of each Cu-mutant complex were carried out, starting from the same minimised structure but with different initial velocities, randomly sampled from the Maxwell-Boltzmann distribution at 310 K. Electrostatic interactions were neglected beyond

a cut-off of 12 Å, and the Generalised Born solvation model used to solvate all systems[46,47,48]: this approach has been shown to enhance conformational sampling of flexible systems. During all simulations, the SHAKE algorithm[49] was used to constrain bonds to hydrogen. Simulations were performed using a 2 fs integration timestep. Equilibration times were taken from RMSD data for all simulations, all pre-equilibrated data from the three 500 ns runs were excluded and the rest was combined to form full individual trajectories to be analysed for all eight systems. This led to around 1.4 μs of data collected for each peptide. Analysis of the trajectories was performed using CPPTRAJ v16.16[50] and VMD 1.9.3[51]. Ramachandran maps were made using MDplot[52] with nomenclature used to describe these from Hollingsworth & Karplus[53].

Results

Root mean square displacement (RMSD) of all backbone atoms relative to starting structure was used as the primary measure of equilibration. Plots of backbone RMSD for each run show that simulations reach stable values after between 5 and 70 ns. All analysis reported is taken from data extracted from frames after these equilibration points,[54] averaged over three separate runs. Once these frames were combined, this led to over 1.4 μs of simulation data collected and analysed for each system. Run A for D7H took the longest amount of time to equilibrate out of all simulations, before reaching a conformational ensemble similar to the other two runs. Averages and standard deviations of RMSD collected over frames after the selected equilibration point (Table 1) confirm equilibration: averages are in the range 2 to 5 Å with standard deviations between 0.3 and 1.2 Å. K16N stands out in this data as being particularly immobile, having the smallest maximum, mean and standard deviation from the starting point. H6R also has small sd, although maximum and mean values are larger than for WT and K16N. Most other mutants exhibit similar properties, A2V is the only simulation with a larger sd value than WT, indicating greater flexibility within this mutant.

Table 1 Statistical analysis of RMSD data (Å)

	Avg	Min	Max	SD
WT	3.84	1.54	6.43	0.80
A2T	3.92	2.04	6.17	0.53
A2V	5.09	2.65	7.18	1.23
H6R	4.57	2.81	6.85	0.29
D7H	3.11	1.77	4.02	0.40
D7N	3.87	2.05	6.37	0.70
E11K	4.08	2.23	5.26	0.52
K16N	2.39	1.30	3.42	0.28

Table 2 reports post-equilibration radius of gyration (Rg) data, which show that on average most mutants are smaller than the wild-type peptide, even in cases where the mutated residue is larger than the one it replaces, such as A2V. E11K has an average value similar to WT: given the larger size of Lys over Glu, this also indicates a compact set of conformations. K16N is particularly small, in accord with low RMSD values noted above, although some of this change may stem from the smaller size of Gln compared to Lys. Standard deviations are small for all cases, further demonstrating the equilibration of the relevant trajectories. D7N exhibits the most variability as well as the largest average size and sd, but amongst mutants there is no obvious relationship between Rg and RMSD data. For instance, in the Rg values for A2V compared to WT suggesting a decrease in size despite its RMSD data. This suggests that the relatively large RMSD value for A2V correspond to motions that do not affect the overall size of the peptide. Solvent accessible surface area (SASA) per residue calculated over post-equilibration trajectories (Table S4) are almost identical for analogous residues between mutants, indicating all residue are fully solvent-exposed.

Table 2 Post equilibration Rg data (Å)

	Avg	Min	Max	SD
WT	7.90	6.77	9.68	0.44
A2T	7.62	6.70	9.66	0.44
A2V	7.37	6.74	8.66	0.24
H6R	7.26	6.75	8.65	0.20
D7H	7.29	6.72	8.21	0.23
D7N	8.14	6.78	9.98	0.49
E11K	7.90	6.90	9.51	0.32
K16N	7.04	6.40	8.74	0.23

Root mean square fluctuation (RMSF) of each residue for all trajectories in each system are reported and illustrated in Figure 3. Although there is substantial scatter in the data, some trends are apparent. The mutated residues themselves do not stand out as having unusual properties: residue 11 in E11K is flexible, but values are high for residue 11 in other systems. N-terminal residues are typically less mobile than C-terminal ones, with residue 16 being particularly flexible in all cases. In agreement with RMSD data, K16N has low RMSF values for all residues. Interestingly, H6R values are also rather low, with the exception of residues 10 & 11 and as mentioned before, residue 16. This agrees with low Rg and RMSD data despite H6R having one of the highest average RMSD values. In contrast, numerous residues in A2V have high RMSF values, but these are not located at or even near the mutation; instead largest values are centred on residues 10-12. Copper-binding residues (1, 6 and 13 for most systems, 1, 13 and 14 for H6R) are among the least mobile, indicating that the metal acts as an “anchor” to bound amino acids. This is especially notable for H6R, suggesting that metal binding to adjacent residues reduces flexibility more than to those that are separated. Bound residues are also notably more rigid in the K16N mutant compared to all other simulations.

It is interesting to note the relative differences in RMSF values between peptides containing mutations at similar positions such as A2T/A2V and D7H/D7N. These proteins with relatively similar amino acid sequences would be expected to display similar figures, yet there is

contrasting data shown between systems for bound residues such as Asp1 which showed variance in RMSF values of 2.33 Å for D7H and 3.33 Å for D7N. As well as this, values differ for both the site of mutation as well as throughout the whole peptide structure displayed in RMSF data for the mutated residues of A2T & A2V of 1.83 and 2.99 Å respectively. In addition, we report a difference of 2.73 Å between values for Val12 and 2.51 Å for Glu11 in these two systems. Reduced incidence of salt-bridges at position Glu11 in A2V allow for increased mobility of residues around this point as shown from the differing values between the two mutant proteins.

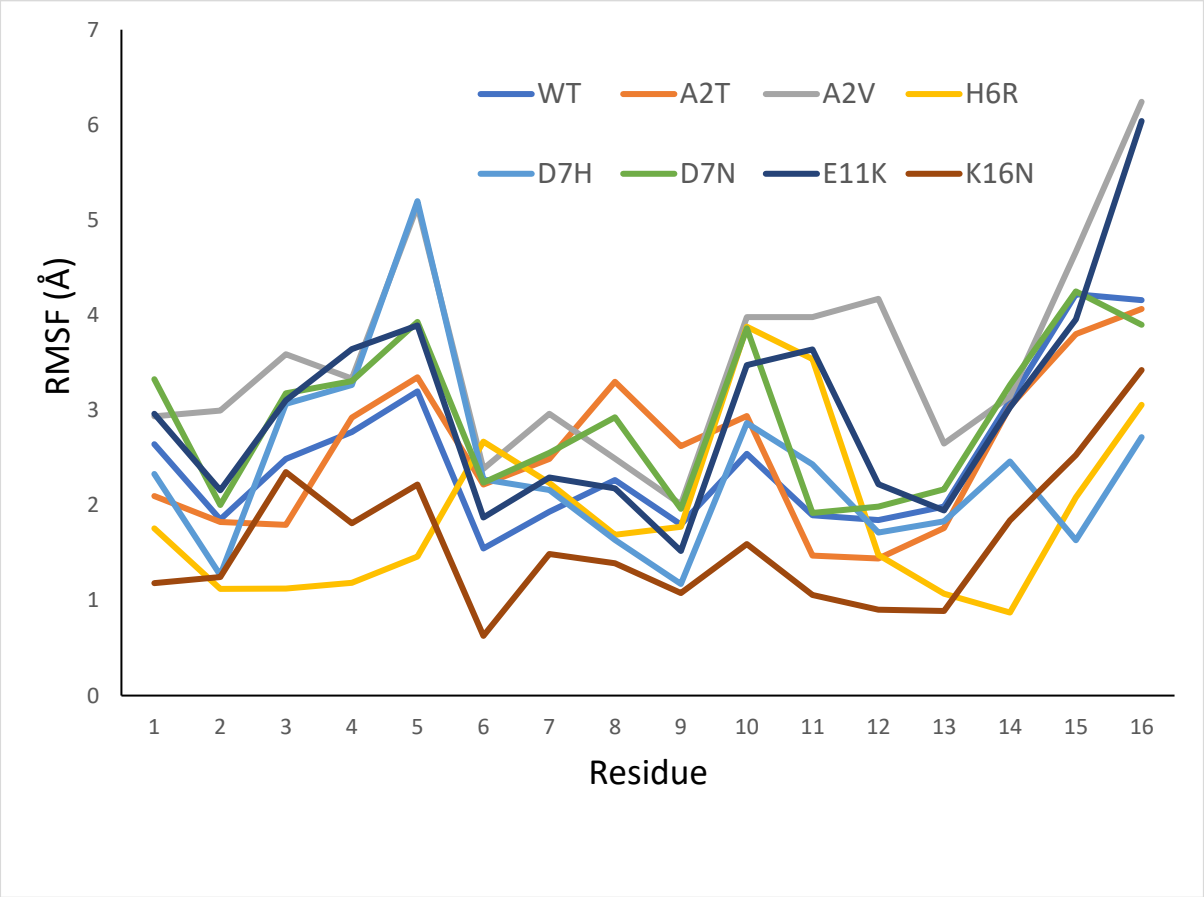

Figure 3 RMSF data per residue (Å)

Clustering further highlights the trends in stability/mobility between mutants: Table 4 reports the number of clusters, and the percentage population of the most and second-most prevalent ones calculated from the DBSCAN clustering algorithm in CPPTRAJ[48]. This shows that K16N in particular, but also H6R, fall into a single dominant cluster, reflecting the

lack of flexibility and variation in RMSD and Rg discussed above. WT and D7H form a relatively highly populated single cluster, albeit with lower prevalence, while A2T, A2V, D7N and E11K fall into several clusters with smaller populations. Views of a representative snapshot of the most populated cluster for each mutant are shown in Figure 4 indicating the change of peptide structure relative to the metal-binding site and site of mutation for all simulations. These show i) the consistency of the metal binding site and ii) the variability and overall lack of defined secondary structure in any given snapshot. The latter is explored in more detail below.

Table 4 Cluster analysis on equilibrated trajectories

Mutant	# Clusters	Most populated (%)	Second Most Populated (%)
WT	10	64.1	1.5
A2T	11	45.9	30.2
A2V	9	32.6	31.5
H6R	7	89.9	5.9
D7H	4	63.8	34.6
D7N	12	49.3	24.1
E11K	16	30.3	28.8
K16N	1	99.8	N/A

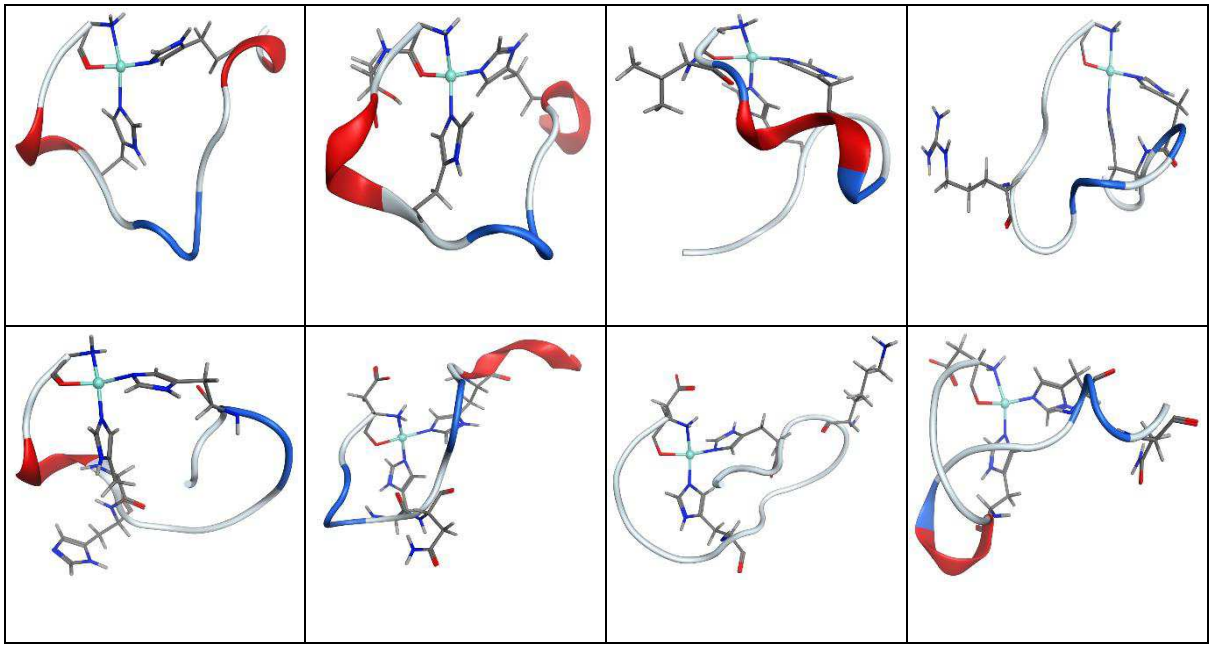

Figure 4 Highest populated clusters for each simulation. Top row (L-R) WT, A2T, A2V, H6R; Bottom Row (L-R) D7H, D7N, E11K, K16N. Cu is represented as the teal ball, relevant atoms on coordinated sites as well as mutated residues are shown as wireframe. Protein back bone is characterised by its secondary structure: red = α-helix, blue = turn & white = random coil.

Structural comparisons were made via (C_α) of the backbones of the two most-prevalent clusters for all peptides using the UCSF Chimera[55] software tool. The most frequently occurring cluster for WT and A2T have RMSD = 0.970Å. These two clusters also showed high similarity to that of the second most-populated cluster for D7N at 0.374Å and 0.905Å respectively: the structures of all 3 are compared in Figure 5.

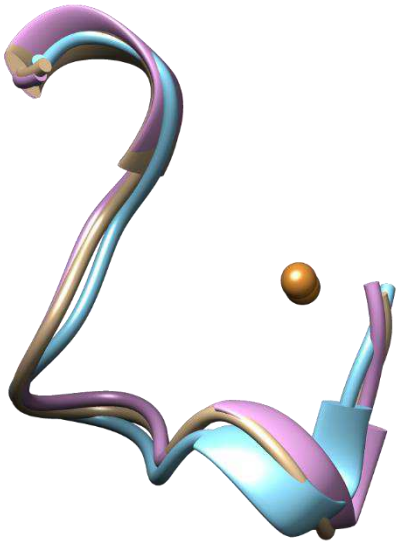

Figure 5- Comparison of C_α on peptide backbones of cluster structures showing highest levels of similarity from RMSD data. **Tan**- WT, **Blue**- A2T, **Purple**- D7N, **Orange Sphere-** Cu

Salt-bridges play an important role in peptide structure: percentage populations of all possible combinations of oppositely charged residues across equilibrated trajectories are displayed in Figure 6. Data shows that all mutations have a strong effect on the number and distribution of salt bridges. Compared to WT, the two mutations that leave the number of charged residues unchanged, A2T and A2V, reduce the frequency of Asp1-Arg5 and increase that of Asp7-Lys16 in A2V, while the incidence of Glu11-Arg5 and Glu11-Lys16 is also diminished in A2V but remain consistent in A2T. Salt-bridge profiles between these two mutants show contrasts in types of interaction and frequency with Glu3-Lys16 and Asp7-Lys16 present in A2V but absent in A2T, whilst Asp1-Lys16 interactions appear only in A2T.

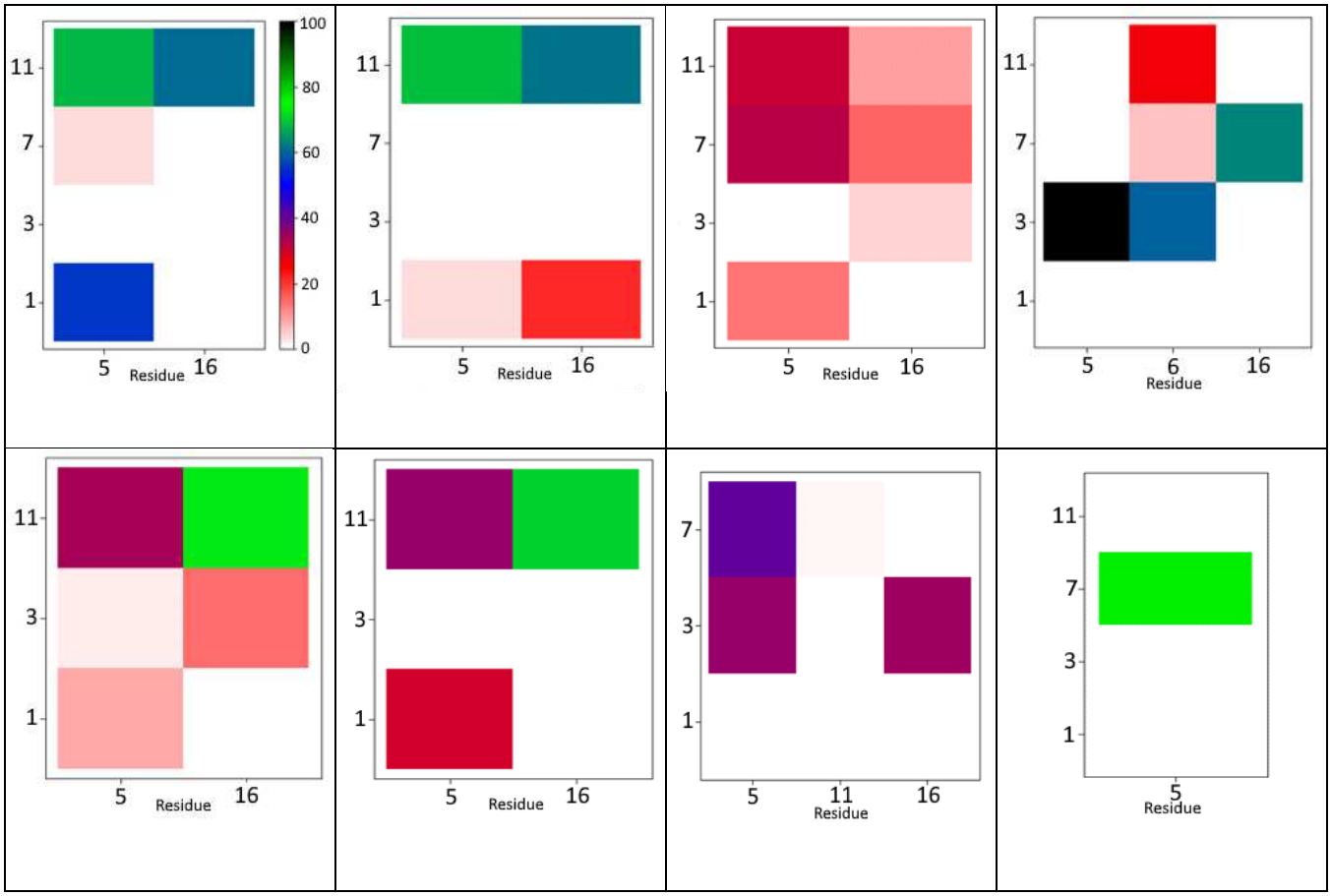

Figure 6- Salt bridge plots by percentage for equilibrated simulations. **Top row (L-R);** WT, A2T, A2V, H6R. **Bottom row (L-R);** D7H, D7N, E11K, K16N.

H6R introduces an extra positively charged residue, which interacts most commonly with Glu3, but also Glu11 and occasionally Asp7. Glu3 is also found in contact with Arg5 for almost every recorded frame: the close proximity of these residues is illustrated in Figure 7, showing that Glu3 bridges between the two adjacent positive residues. The presence of Arg6 also acts to remove completely the interactions of Arg5 with both Asp1 and Glu11, and also the Glu11-Lys16 link, that were prevalent in WT.

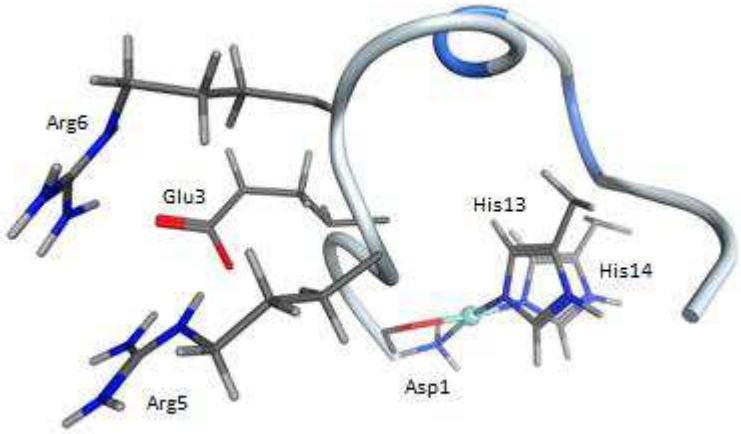

Figure 7- View of H6R, with sidechains of Glu3, Arg5 and Arg6, along with metal binding site, shown as wireframe, and the backbone of the remaining peptide as a ribbon

In contrast, D7N and D7H remove a negatively charged residue: however, Asp7 is not heavily involved in salt bridges in WT, such that the pattern of salt bridge population is closest to WT for these mutants. Some changes are still evident, such as a reduction in the interactions of Asp1, with concomitant increase in contacts to Glu3 in D7H. The two mutations of Asp7 show a decrease in the occurrence of Glu11-Arg5 and an increase in Glu11-Lys16 salt-bridges compared to WT but remain consistent with each other at relatively similar levels of incidence.

E11K swaps the sign of residue 11: the introduced positive sidechain does not engage in any significant interactions. The loss of Glu11 leads to changes in interactions of Arg5 and Lys16, especially with Glu3, and also to the complete loss of interactions of Asp1. K16N removes a positive residue, leaving only Arg5, which forms a highly populated bridge to Asp7, but no other significantly populated interactions. Across all the simulations, the most commonly observed salt bridge is that between Glu11-Lys16, at 46% of all possible frames, while Asp1-Lys16 is observed for only 3.2% of the full set of equilibrated trajectories.

Contact maps show average distances (Å) between C_α within the peptide backbone per residue (Figure 8). These maps reflect the patterns in flexibility noted above: for instance, the least mobile peptides K16N and D7H display large areas of short contact (blue in Figure 8), whereas the most flexible ones W2T, A2T and D7N exhibit large areas of longer average

contacts (orange/red in Figure 8). However, the precise pattern of contacts varies: short contacts between Ala2-His6 and Tyr10-Glu11 are present in K16N, while the closest contacts in D7H are between Gln15-Lys16 and His6-Tyr10. High incidences of salt-bridges formed such as with Glu3-Arg5 in E11K are also seen as short distances contact maps.

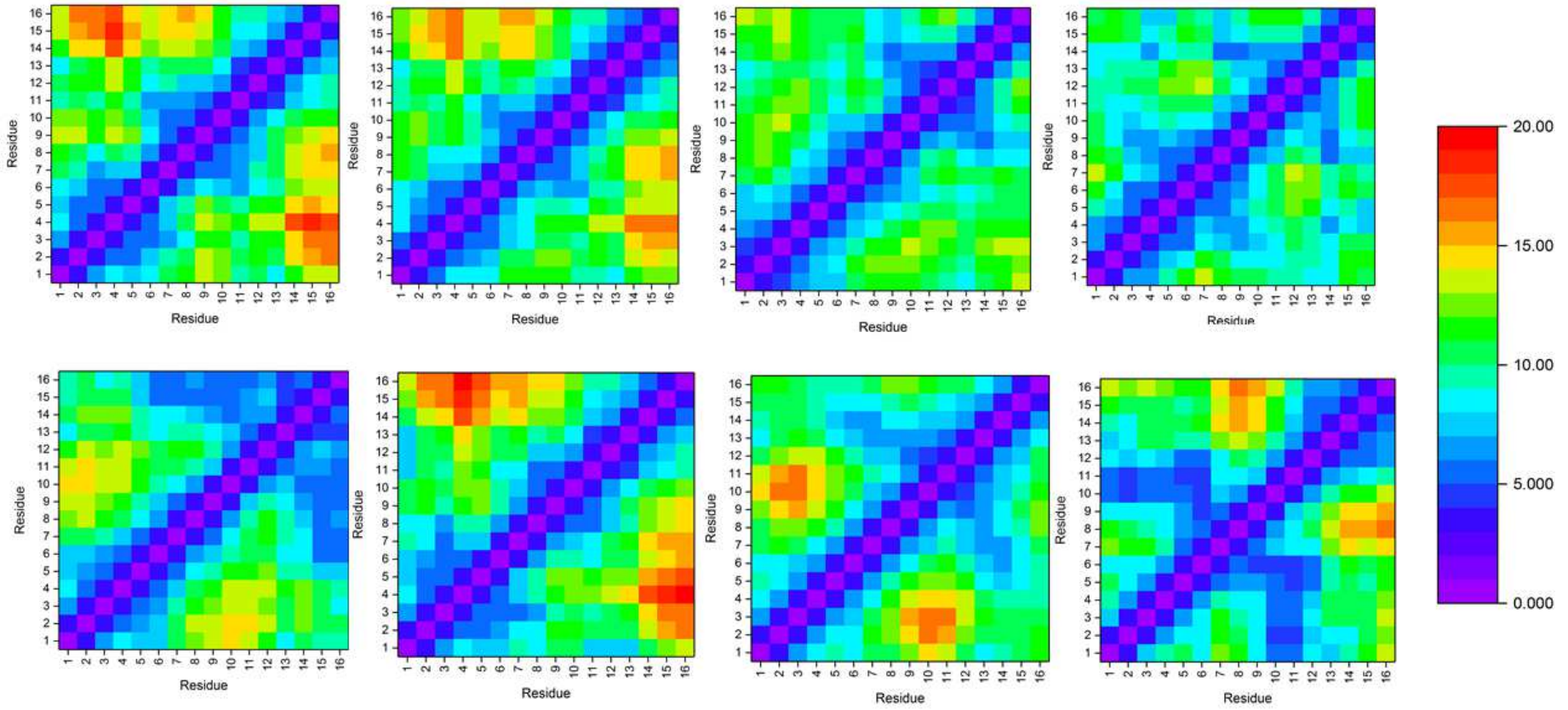

Figure 8 Contact map of average distance between C_α (Å). **Top row (L-R)**; WT, A2T, A2V, H6R. **Bottom row (L-R);** D7H, D7N, E11K, K16N.

Ramachandran plots for all post-equilibration frames for all mutants are shown in Figure 9. In WT, the highest incidence is found within the α-region, centred on ϕ, ψ = -63, -43, followed by P_{II} (-105, 100 to -30, 200) and β (-180, 90 to -105, 190), as well as some δ' character (35, 60 to 100, -25), at similar levels to those found in the β region. A2T, A2V, and H6R have similar Ramachandran maps, showing increased population of P_{II} and reduced of α, whilst maintaining relatively similar levels of β character to WT. D7H differs from the others, as both the P_{II} and α regions are equally populated, and also as the only plot to possess a significant amount of character within the δ region (-30, -65 to -135, 40).

D7N differs from D7H showing less P_{II} character than its Asp7 counterpart as well as an increase in δ' making it the most comparable plot to WT. E11K has similar level of P_{II} and α, with less β character than others considered. This plot also has the most incidence of conformations with positive ϕ, which for non-glycine residues is usually an indicator of steric hindrance. K16N is broadly similar to WT, with most residues located within the α-region, but this mutant lacks any P_{II} character, with greater population of the β-region, albeit spread out over a broader distribution then seen in the other plots.

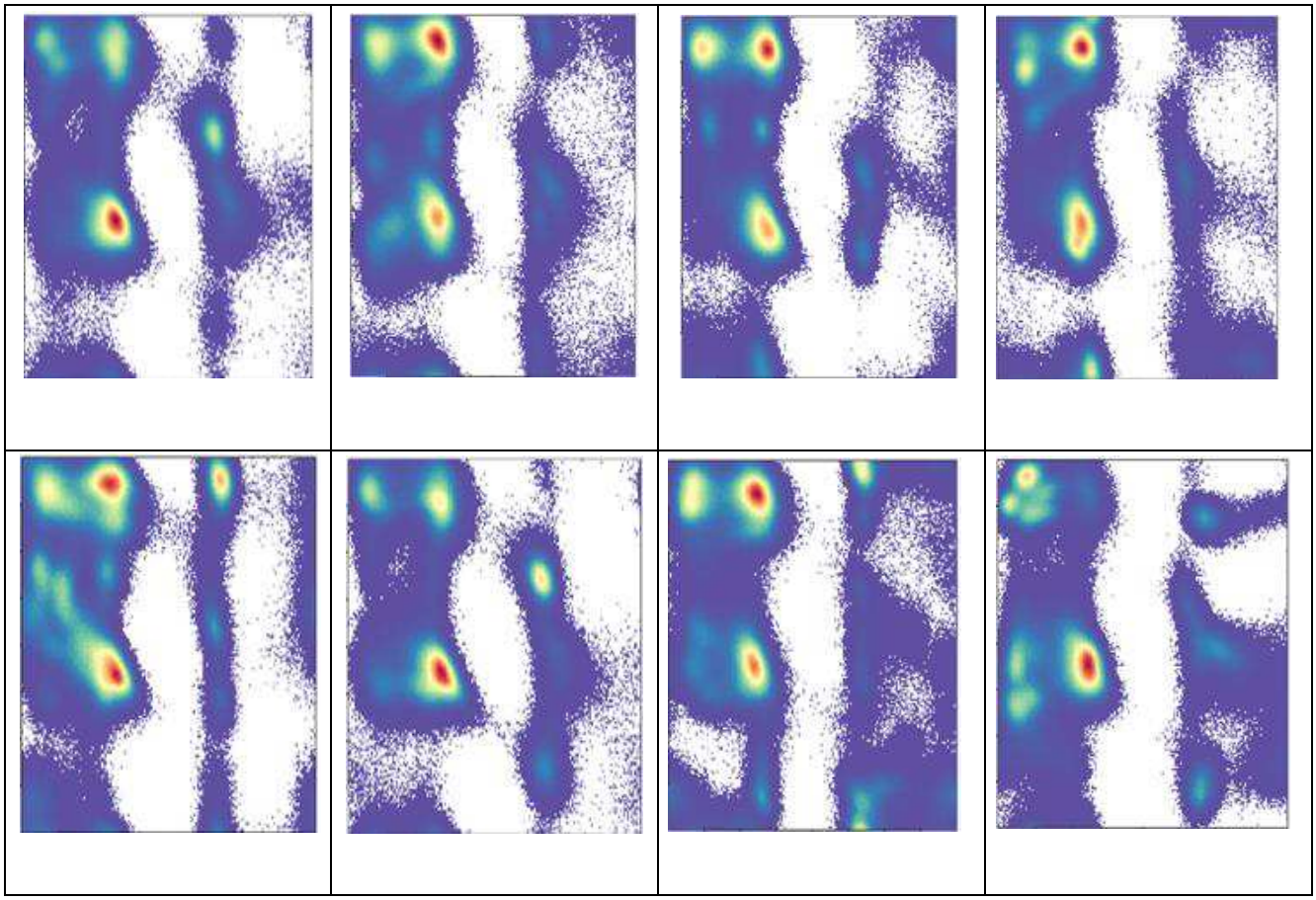

Figure 9- Ramachandran plots for equilibrated trajectories. **Top row (L-R)**; WT, A2T, A2V, H6R. **Bottom row (L-R);** D7H, D7N, E11K, K16N. Red areas indicate most prevalent character, blue regions indicate lower levels of incidence and white is an absence of character. X-axis = ϕ[°], y-axis = ψ[°].

The effect of mutations on secondary structure are marked and varied, as shown in Table 5. WT is characterised by a large amount of coil (at termini) and turn (residues 3-5 and 8-10), along with 3,10 helices and some β-strand but almost no α-helix. This is apparently at odds with the Ramachandran plot for WT above, which shows high concentration of frames lying in the region associated with α-helical structure. It is, however, in accord with Hollingsworth and Karplus's finding that residues that are not classified as helical are still found in this region of ϕ-ψ space, and are perhaps better thought of as belonging to "an extended δ-region".

A2T shows the greatest increase in helical character over the whole sequence whilst losing some of its β-character, whereas A2V only displays α-helix across residues 3-7 as well as an increase in β-strand content. H6R exhibits very little helix or strand structure, being

dominated by coil/turn/bend structure with only small elements of 3,10-helix and strand located mainly between residues 6-10.

D7H shares similarities to WT, albeit with greater proportions of β-strand. D7N and D7H are closest in resemblance to each other in terms of α-content despite notable variances in salt-bridge profiles suggesting a difference in structures. In D7H, the presence of helical geometry is limited to residues 3-6 whilst D7N displays this between 3-5 but also towards the C-termini between residues 13-16. The percentage of strand character differs between these two mutant systems with D7H displaying β-characteristics over a larger range of residues than D7N.

E11K displays almost no helix content and predominantly forms coil/turn/bend formations making up the predominant character of its secondary structure. K16N leads to strand content closer to the N-terminus and helices at the C-terminus at incidence levels comparable to that of WT. No clear pattern of changes in the mutated residues themselves is found, such that changes to secondary structure are global rather than local.

Table 5 Percentage of residues classified as helical, strand, or other

	Helix	Strand	Other
WT	14.5	2.4	83.1
A2T	31.0	0.5	68.5
A2V	8.9	4.2	86.9
H6R	3.6	0.3	96.1
D7H	11.4	7.2	81.4
D7N	11.6	1.3	87.1
E11K	<0.1%	4.9	95.0
K16N	13.8	3.9	82.3

Average binding energies of Cu(II) to each peptide were calculated using the semi-empirical GFN2-xTB method, and reported in Table 7. Structures were taken every 100 ns from all 8 equilibrated trajectories of approximately 1.4 μs and minimised, before calculation of the total energy of Cu-peptide complex + 4(H_2O) compared to the free peptide and $[Cu(H2O)4]^{2+}$, all in implicit model of aqueous solvent. No major conformational changes

were observed following optimisation shown by RMSD values comparing structures generated in AMBER and minimised structures from xTB.

Most binding energies are typically in the range of -70 to -110 kJ mol^{-1}, indicating that most peptides considered have similar affinities for binding with copper ions. H6R is one of the closest in binding energy to WT, despite possessing an extra positively charged residue and a different mode of bonding from all other simulations. However, Cu(II) is more strongly bound to WT, whereas binding to K16N is markedly weaker than all other systems with binding energy of -30 kJ mol^{-1}. All mutant peptides had a lower average difference in binding energy compared to the WT showing weaker binding to the metal centre. Relatively high standard deviations indicate a wide range of values for binding energies for all mutant simulations indicating a high level of variability across trajectories. Average binding energies are displayed with standard deviations in Figure 10.

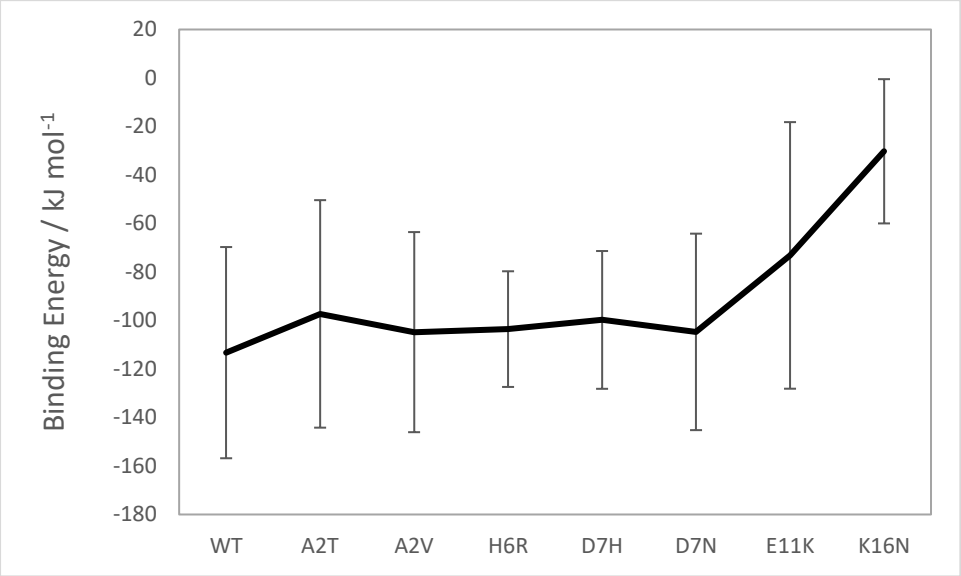

Figure 10- Binding energies with standard deviations for each mutant

Discussion

MD simulations of Cu-complexes of N-terminal mutants yielded evidence that the effects of point mutations of Aβ vary significantly and depend on the site of mutation as well as the specific amino acids involved. We find marked differences between mutants in secondary structure, conformations adopted, and flexibility/stability.

Within the mutations that do not alter charge state, *i.e.* A2V and A2T, greater flexibility was observed in A2V compared to WT, despite it adopting more compact conformations, as shown by Rg data. In conjunction with RMSF results, we observed that the greatest contribution to this more mobile nature occurs after Tyr10 peptide, but increased movement was noted across entire structure. A2T however, displayed less flexibility than both A2V and WT in addition to adopting conformations comparable in size to WT shown via similar Rg values. Additionally, A2T showed less mobility in its RMSF values after Tyr10 in direct contrast to A2V due to a notable decrease in formation of salt-bridges with Glu11 in the latter. Trajectories for these mutants fall into a similar number of clusters as the WT, albeit with more evenly distributed population, further confirming their dynamic nature. As charge is unchanged and sequences relatively similar, we expected to see similar salt-bridge profiles. Instead, the incidence and combinations of these attractive forces displayed notable differences from the WT protein and each other, with only Glu11 interactions remaining consistent between WT and A2T. Several salt-bridges formed in the A2T and A2V simulations were rather transient, further demonstrating the constant fluctuation of atoms and residues in these systems over the course of the simulations.

H6R and K16N are similar in terms of structure and stability. RMSD and Rg data show they adopt more rigid and compact conformations compared to WT, with lower RMSF values per residue, demonstrating the stability of these mutated peptides. Further evidence of this is exhibited in cluster analysis: both adopt a single prevalent structure over the course of their simulations. Addition of a positive residue in H6R peptide was expected to yield an increase in salt-bridge formation at Arg6, which was indeed found. However, some salt-bridges present in WT are lost completely while new ones are observed remotely from the site of mutation. In contrast, K16N loses a positive residue and thus has reduced potential for salt-bridges, evident in the fact that only one such interaction forms for an appreciable time, suggesting that the stability of this mutant cannot be accounted for by these forces. The Ramachandran plot lacks P_{II} character, present in all other simulations, but shows increased presence of organised α and β-character, which may be the origin of the relative stability.

D7H and D7N mutants have contrasting properties, unanticipated for two different mutations at the same site, including RMSD and Rg compared to WT, indicating they possess different structures. D7N being more comparable to WT than D7H which is much lower for

both RMSD and Rg indicating it possesses a more rigid, compact set of conformations. RMSF data clearly shows the differences between these peptides: values for residues in D7N are consistently higher than WT across the whole peptide, whereas D7H has values generally similar to or much lower than WT especially in residues towards the C-terminus. This is also evident in clustering data, which indicate D7H populates fewer conformations than D7N, which is more comparable to the A2T/A2V systems, occupying a greater number of more sparsely populated clusters. These differences between systems are also seen in Ramachandran plots: D7H has an even distribution between P_{II} and α regions, as well as significant γ-character, whereas D7N has a Ramachandran plot comparable to WT with similar population of P_{II}, α, and even δ' consistent with the unmutated peptide. Mutation of Asp7 was not expected to strongly affect salt-bridges, as this residue is barely involved in these interactions in WT. However, this was not the case with significant differences in nature and incidence of interactions. Glu-11 interactions were consistent with one another but at different levels to WT, additionally no other salt-bridges formed at significant levels in these two mutant systems.

E11K adopts a less rigid conformation than the other peptides simulated. Average Rg for this system is the same as WT, but the increased size of Lys means that E11K adopts a more compact structure than the WT overall. Despite this, RMSF data is greater for all residues in E11K compared to WT, indicating greater flexibility. Additionally, this mutant forms the highest number of clusters. This particular variant substitutes a positive residue for a negative one, but the new Lys forms no significant salt-bridge interactions, and also eliminates all salt-bridges of Asp1 that were present in WT. The Ramachandran plot for this structure displays a significant population in the positive ϕ side, usually indicative of steric hindrance, which could be the origin of the flexibility of this mutant.

Overall, a decrease in helical character was observed in all simulations compared to WT except A2T: some mutants lose nearly all helical structure, such as E11K, whereas formation of helices increased in A2T by more than double. Increased β-character was recorded in most simulations, with the exceptions of A2T, H6R, and D7N which saw a decrease or similar levels of β-strand structures compared to WT. Previous studies have shown a link between β-character and enhanced aggregational properties[56]. The lack of β-strands in simulation data for A2T, provides supporting evidence for the protective nature of this mutant[57]. H6R,

D7H, and D7N have been shown in similar MD simulations[58] to form an increased level of β-character which held true for the D7H simulation data we report. It can be expected that the monomeric forms of mutant species reported here may not generate results indicative of those observed in oligomeric species associated with enhanced neurotoxicity and aggregation[59] however the results we have generated for the truncated species seem to be in agreement with similar MD experiments on larger Aβ peptides.

D7H and D7N were most comparable to one another, despite their contrasting results in other analyses, whereas K16N was most similar to the unaltered WT peptide. We find that the effects of mutations on peptide structure is global as opposed to local, as evident in from the varied salt-bridge profiles for each mutant, which exhibit changes in interactions and structures remote to the site of mutation in all analysis. Ramachandran plots and secondary structure analysis show distinct differences and similarities between systems and highlight the contrasts in structure between comparable mutations at a similar location such as A2T/A2V and D7H/D7N.

Conclusions

In this study, we used MD simulations to explore the effects of N-terminus genetic mutations on the truncated Aβ 1-16 peptide when bound with Cu(II), with the aim of finding differences between mutants and drawing comparisons of these variants with the WT peptide. Literature data indicates varying effects on pathogenicity and structure between mutants. All mutants varied in terms of rigidity and size, as seen in RMSD and Rg data comparable to WT as well as one another, showing these mutations have differing effects on morphology of the Aβ peptide. We observed conformational changes between each system from this data in conjunction with cluster analysis showing varying degrees of mobility.

Results for different mutations at similar locations were independent of each other, showing some similarities as well as distinctions between systems such as D7H compared to D7N. From this it can be ascertained that both the location and type of mutation that alters the structure of the peptide. Salt-bridge data was markedly varied between simulations and in conjunction with Ramachandran plots showing different profiles for each mutant, showed

that the changes are not local to the site of mutation, and that overall structure should be considered when comparing such systems.

In nearly all cases, the levels of helical character decreased in comparison to WT, forming either more β-character or coil/turn/bend. Previous studies have shown an increase in β-sheets have been the driving force for aggregation. It is interesting to note that the decrease in β-character observed in A2T is in agreement with the previously reported protective nature of this mutation[19]. E11K and A2V display an increase in β-strand like structures which was expected due to their reported pathogenicity[16,17]. Despite our simulations only being performed on the truncated, monomeric peptides, the MD results reported indicate that these are effective models of the full-length Aβ and inferences of the effects of these genetic mutations can still be made from this data. We hope to report analogous data for C-terminal mutants on the full peptide in due course. The impact of mutations on aggregation properties could be explored further by using MD to further model peptides dimers or oligomers in systems that closer replicate those *in vivo*.

Supporting Information

Plots of RMSD and Rg over time, equilibration times, numerical salt bridge data is available as Electronic Supporting Information. Trajectories, in the form of PDB files, for all runs are available from DOI 10.5281/zenodo.3548346

Acknowledgements

NAS is grateful to the Saudi Arabian Ministry of Higher education and Cultural Bureau in London funding. The authors gratefully acknowledge the Super Computing Wales facility for access.

References

1 What is Alzheimer's | Alzheimer's Association, https://alz.org/alzheimers-dementia/what-is-alzheimers, (accessed 14 November 2018).

2 G. McKhann, D. Drachman, M. Folstein, R. Katzman, D. Price and E. Stadlan, *Neurology*, 1984, **34**, 939–944.

3 Cleusa P Ferri, Martin Prince, Carol Brayne, Henry Brodaty, Laura Fratiglioni, Mary Ganguli, Kathleen Hall, Kazuo Hasegawa, Hugh Hendrie, Yueqin Huang, Anthony Jorm, Colin Mathers, Paulo R Menezes, Elizabeth Rimmer and Marcia Scazufca, *Lancet*, 2005, **366**, 2112–17.

4 R. A. Stelzmann, H. N. Schnitzlein and F. R. Murtagh, *Clin. Anat.*, 1995, **8**, 429–43.

5 D. Greene, T. Po, J. Pan, T. Tabibian and R. Luo, *J. Phys. Chem. B*, 2018, **122**, 4521–4536.

6 B. Alies, H. Eury, C. Bijani, L. Rechignat, P. Faller and C. Hureau, *Inorg. Chem.*, 2011, **50**, 11192–11201.

7 S. Wärmländer, A. Tiiman, A. Abelein, J. Luo, J. Jarvet, K. L. Söderberg, J. Danielsson and A. Gräslund, *ChemBioChem*, 2013, **14**, 1692–1704.

8 S. C. Drew, C. J. Noble, C. L. Masters, G. R. Hanson and K. J. Barnham, *J. Am. Chem. Soc.*, 2009, **131**, 1195–1207.

9 C. B. Eckman and E. A. Eckman, *Neurol Clin.*, 2007, **25**, 669–679.

10 A. F. Teich and O. Arancio, *Biochem. J.*, 2012, **446**, 165–177.

11 B. Jiao, B. Tang, X. Liu, J. Xu, Y. Wang, L. Zhou, F. Zhang, X. Yan, Y. Zhou and L. Shen, *Neurobiol. Aging*, 2014, **35**, 1957.e1-1957.e6.

12 C. Ballard, S. Gauthier, A. Corbett, C. Brayne, D. Aarsland and E. Jones, *Lancet*, 2011, **377**, 1019–1031.

13 APP | ALZFORUM, https://www.alzforum.org/mutations/app, (accessed 17 November 2018).

14 S. Weggen and D. Beher, *Alzheimer's Res. Ther.*, 2012, 4.

15 K. P. Kepp, *Coord. Chem. Rev.*, 2017, **351**, 127–159.

16 L. Zhou, N. Brouwers, I. Benilova, A. Vandersteen, M. Mercken, K. Van Laere, P. Van Damme, D. Demedts, F. Van Leuven, K. Sleegers, K. Broersen, C. Van Broeckhoven, R. Vandenberghe and B. De Strooper, *EMBO Mol. Med.*, 2011, **3**, 291–302.

17 G. Di Fede, M. Catania, M. Morbin, G. Rossi, S. Suardi, G. Mazzoleni, M. Merlin, A. R. Giovagnoli, S. Prioni, A. Erbetta, C. Falcone, M. Gobbi, L. Colombo, A. Bastone, M. Beeg, C. Manzoni, B. Francescucci, A. Spagnoli, L. Cantu, E. Del Favero, E. Levy, M. Salmona and F. Tagliavini, *Science (80-.).*, 2009, **323**, 1473–1477.

18 D. Kaden, A. Harmeier, C. Weise, L. M. Munter, V. Althoff, B. R. Rost, P. W. Hildebrand, D. Schmitz, M. Schaefer, R. Lurz, S. Skodda, R. Yamamoto, S. Arlt, U. Finckh and G. Multhaup, *EMBO Mol. Med.*, 2012, **4**, 647–659.

19 B. Murray, M. Sorci, J. Rosenthal, J. Lippens, D. Isaacson, P. Das, D. Fabris, S. Li and G. Belfort, *Proteins Struct. Funct. Bioinforma.*, 2016, **84**, 488–500.

20 J. A. Duce and A. I. Bush, *Prog. Neurobiol.*, 2010, **92**, 1–18.

21 K. I. Silva, B. C. Michael, S. J. Geib and S. Saxena, *J. Phys. Chem. B*, 2014, **118**, 8935–8944.

22 V. Balland, C. Hureau and J.-M. Savéant, 2010, 5, 17113–17118.

23 Y. H. Hung, A. I. Bush and R. A. Cherny, *J. Biol. Inorg. Chem.*, 2010, 15, 61–76.

24 A. I. Bush and R. E. Tanzi, *Therapeutics for Alzheimer's Disease Based on the Metal Hypothesis*, 2008.

25 A. I. Bush, *Trends Neurosci.*, 2003, 26, 207–214.

26 S. Karantzoulis and J. E. Galvin, *Expert Rev. Neurother.*, 2011, 11, 1579–1591.

27 M. A. Lovell, J. D. Robertson, W. J. Teesdale, J. L. Campbell and W. R. Markesbery, *J. Neurol. Sci.*, 1998, **158**, 47–52.

28 V. Tõugu, A. Karafin, K. Zovo, R. S. Chung, C. Howells, A. K. West and P. Palumaa, *J.*

Neurochem., 2009, **110**, 1784–1795.

29 C. Cheignon, M. Jones, E. Atrián-Blasco, I. Kieffer, P. Faller, F. Collin and C. Hureau, *Chem. Sci.*, 2017, **8**, 5107–5118.

30 V. I. Polshakov, A. B. Mantsyzov, S. A. Kozin, A. A. Adzhubei, S. S. Zhokhov, W. van Beek, A. A. Kulikova, M. I. Indeykina, V. A. Mitkevich and A. A. Makarov, *Angew. Chemie - Int. Ed.*, 2017, **56**, 11734–11739.

31 M. H. Viet, P. H. Nguyen, S. T. Ngo, M. S. Li and P. Derreumaux, *Acs Chem. Neurosci.*, 2013, **4**, 1446–1457.

32 Y. Hori, T. Hashimoto, Y. Wakutani, K. Urakami, K. Nakashima, M. M. Condron, S. Tsubuki, T. C. Saido, D. B. Teplow and T. Iwatsubo, *J. Biol. Chem.*, 2007, **282**, 4916–4923.

33 L. K. Simmons, P. C. May, K. J. Tomaselli, R. E. Rydel, K. S. Fuson, E. F. Brigham, S. Wright, I. Lieberburg, G. W. Becker and D. N. Brems, *Mol. Pharmacol.*, 1994, **45**, 373–9.

34 J. Alí-Torres, J. D. Maréchal, L. Rodríguez-Santiago and M. Sodupe, *J. Am. Chem. Soc.*, 2011, **133**, 15008–15014.

35 S. Furlan, C. Hureau, P. Faller and G. La Penna, *J. Phys. Chem. B*, 2010, **114**, 15119–15133.

36 *Molecular Operating Environment (MOE),* 2013.08; Chemical Computing Group ULC, 1010 Sherbrooke St. West, Suite #910, Montreal, QC, Canada, H3A 2R7, 2018.

37 E. Atrián-Blasco, M. Del Barrio, P. Faller and C. Hureau, *Anal. Chem.*, 2018, **90**, 5909–5915.

38 B. Alies, H. Eury, C. Bijani, L. Rechignat, P. Faller and C. Hureau, *Inorg. Chem.*, 2011, **50**, 11192–11201.

39 P. Labute, *J. Chem. Inf. Model.*, 2010, **50**, 792–800.

40 D.A. Case, R.M. Betz, D.S. Cerutti, T.E. Cheatham, III, T.A. Darden, R.E. Duke, T.J. Giese, H. Gohlke, A.W. Goetz, N. Homeyer, S. Izadi, P. Janowski, J. Kaus, A. Kovalenko,

T.S. Lee, S. LeGrand, P. Li, C. Lin, T. Luchko, R. Luo, B. Madej, D. Mermelstein, K.M. Merz, G. Monard, H. Nguyen, H.T. Nguyen, I. Omelyan, A. Onufriev, D.R. Roe, A. Roitberg, C. Sagui, C.L. Simmerling, W.M. Botello-Smith, J. Swails, R.C. Walker, J. Wang, R.M. Wolf, X. Wu, L. Xiao and P.A. Kollman (2016), AMBER 2016, University of California, San Francisco.

41 J. A. Maier, C. Martinez, K. Kasavajhala, L. Wickstrom, K. E. Hauser and C. Simmerling, *J. Chem. Theory Comput.*, 2015, **11**, 3696–3713.

42 P. Li and K. M. Merz, *J. Chem. Inf. Model.*, 2016, **56**, 599–604.

43 M. J. Frisch, G. W. Trucks, H. B. Schlegel, G. E. Scuseria, M. A. Robb, J. R. Cheeseman, G. Scalmani, V. Barone, G. A. Petersson, H. Nakatsuji, X. Li, M. Caricato, A. Marenich, J. Bloino, B. G. Janesko, R. Gomperts, B. Mennucci, H. P. Hratchian, J. V. Ortiz, A. F. Izmaylov, J. L. Sonnenberg, D. Williams-Young, F. Ding, F. Lipparini, F. Egidi, J. Goings, B. Peng, A. Petrone, T. Henderson, D. Ranasinghe, V. G. Zakrzewski, J. Gao, N. Rega, G. Zheng, W. Liang, M. Hada, M. Ehara, K. Toyota, R. Fukuda, J. Hasegawa, M. Ishida, T. Nakajima, Y. Honda, O. Kitao, H. Nakai, T. Vreven, K. Throssell, J. A. Montgomery, Jr., J. E. Peralta, F. Ogliaro, M. Bearpark, J. J. Heyd, E. Brothers, K. N. Kudin, V. N. Staroverov, T. Keith, R. Kobayashi, J. Normand, K. Raghavachari, A. Rendell, J. C. Burant, S. S. Iyengar, J. Tomasi, M. Cossi, J. M. Millam, M. Klene, C. Adamo, R. Cammi, J. W. Ochterski, R. L. Martin, K. Morokuma, O. Farkas, J. B. Foresman, and D. J. Fox, Gaussian, Inc., Wallingford CT, 2016

44 C. Bannwarth, S. Ehlert and S. Grimme, *J. Chem. Theory Comput.*, 2019, **15**, 1652–1671.

45 GitHub/grimme-lab/xtb, https://github.com/grimme-lab/xtb/, (accessed 14 November 2019).

46 W. Clark Still, A. Tempczyk, R. C. Hawley and T. Hendrickson, *J. Am. Chem. Soc.*, 1990, **112**, 6127–9.

47 R. Constanciel and R. Contreras, *Theor. Chim. Acta*, 1984, **65**, 1–11.

48 M. Schaefer and M. Karplus, *J. Phys. Chem.*, 1996, **100**, 1578–1599.

49 J. P. Ryckaert, G. Ciccotti and H. J. C. Berendsen, *J. Comput. Phys.*, 1977, **23**, 327–341.

50 D. R. Roe and T. E. Cheatham, *J. Chem. Theory Comput.*, 2013, **9**, 3084–3095.

51 W. Humphrey, A. Dalke and K. Schuten, 1996, 33–38.

52 C. Margreitter and C. Oostenbrink, 2017, **9**, 164–186.

53 S. A. Hollingsworth and P. A. Karplus, *Biomol. Concepts*, 2010, **1**, 271–283.

54 P. D. Q. Huy, Q. Van Vuong, G. La Penna, P. Faller and M. S. Li, *ACS Chem. Neurosci.*, 2016, **7**, 1348–1363.

55 E. F. Pettersen, T. D. Goddard, C. C. Huang, G. S. Couch, D. M. Greenblatt, E. C. Meng and T. E. Ferrin, *J. Comput. Chem.*, 2004, **25**, 1605–1612.

56 G. G. Glenner and C. W. Wong, *Biochem. Biophys. Res. Commun.*, 1984, **120**, 885–890.

57 J. A. Maloney, T. Bainbridge, A. Gustafson, S. Zhang, R. Kyauk, P. Steiner, M. Van Der Brug, Y. Liu, J. A. Ernst, R. J. Watts and J. K. Atwal, *J. Biol. Chem.*, 2014, **289**, 30990–31000.

58 L. Xu, Y. Chen and X. Wang, *Proteins Struct. Funct. Bioinforma.*, 2014, **82**, 3286–3297.

59 K. Ono, M. M. Condron and D. B. Teplow, *J. Biol. Chem.*, 2010, **285**, 23186–23197.